Geophysical Research Letters®

RESEARCH LETTER
10.1029/2025GL115520

Mesoscale Induced Vertical Fluxes Over the Iceland-Faroe Ridge

Charly de Marez[1], **Angel Ruiz-Angulo**[1], **and Jonathan Gula**[2,3]

[1]University of Iceland, Reykjavik, Iceland, [2]Laboratoire d'Océanographie Physique et Spatiale (LOPS), University Brest, CNRS, Ifremer, IRD, IUEM, Plouzané, France, [3]Institute Universitaire de France (IUF), Paris, France

Key Points:

- SWOT altimetry reveals energetic mesoscale eddies on the Iceland-Faroe Ridge
- High-resolution numerical modeling shows these eddies induce intense vertical heat fluxes
- Vertical heat fluxes likely contribute to the warming of bottom waters

Supporting Information:

Supporting Information may be found in the online version of this article.

Correspondence to:

C. de Marez,
charly@hi.is

Citation:

de Marez, C., Ruiz-Angulo, A., & Gula, J. (2025). Mesoscale induced vertical fluxes over the Iceland-Faroe ridge. *Geophysical Research Letters*, *52*, e2025GL115520. https://doi.org/10.1029/2025GL115520

Received 25 FEB 2025
Accepted 16 JUN 2025

Author Contributions:

Conceptualization: Charly de Marez
Formal analysis: Angel Ruiz-Angulo, Jonathan Gula
Funding acquisition: Angel Ruiz-Angulo
Investigation: Charly de Marez
Methodology: Charly de Marez
Project administration: Angel Ruiz-Angulo
Resources: Angel Ruiz-Angulo, Jonathan Gula
Software: Jonathan Gula
Visualization: Charly de Marez
Writing – original draft: Charly de Marez
Writing – review & editing: Charly de Marez, Angel Ruiz-Angulo, Jonathan Gula

Abstract Mesoscale eddies play a crucial role in ocean dynamics, yet their impact on vertical heat fluxes over topographic features remains poorly understood. This study investigates the Iceland-Faroe Ridge (IFR), a key boundary between the North Atlantic and Nordic Seas, southeast of Iceland. A warming of surface waters of 1°C over the past 40 years in the region has shifted thermal structures, potentially impacting the upper cell of the global thermohaline circulation. Using newly available high-resolution SWOT altimetry and numerical modeling, we directly observe mesoscale turbulence atop the IFR for the first time and quantify its role in driving significant vertical heat fluxes. This turbulence provides a pathway for heat transfer from warming surface waters to the deep Iceland-Scotland Overflow Water, likely contributing to its observed warming over the past four decades. These findings highlight the critical role of mesoscale dynamics in heat redistribution and the need for enhanced monitoring in this climatically sensitive region.

Plain Language Summary The ocean around Iceland plays a key role in moving heat and shaping the global climate. Small swirling currents, called eddies, help mix ocean heat, but their impact near underwater ridges is not well understood. As ocean temperatures rise rapidly in this region, understanding these processes is crucial. Our study focuses on the Iceland-Faroe Ridge, an underwater boundary between the North Atlantic and Nordic Seas. Using new high-resolution satellite data, we observed these swirling currents in detail for the first time and measured how they move heat vertically. We found that these currents create a direct pathway between warming surface waters and colder deep waters below, likely contributing to deep-water warming observed over the past 40 years. This discovery highlights the critical role of these currents in transferring heat and underscores the need for better monitoring to understand how ocean changes will impact climate and marine ecosystems.

1. Introduction

The Greenland-Scotland Ridge (GSR) is a major topographic feature separating the North Atlantic from the Nordic Seas. While water-mass transformation in the Nordic Seas north of the GSR contributes significantly to the lower limb of the Atlantic Meridional Overturning Circulation (AMOC, Lozier et al., 2019; Chafik & Rossby, 2019), the exchange across the ridge is strongly limited by the shallow topography. Channels, troughs and sills within the GSR are therefore the main pathways for dense waters from the Nordic Seas into the North Atlantic. The GSR naturally separates into three segments due to outcropping islands. The deepest sills are located at either end, in the Faroe Bank Channel (850 m, Blindheim, 1990) east of the Faroe Islands and in the Denmark Strait (620 m, Blindheim, 1990) west of Iceland. The Iceland-Faroe Ridge (IFR) constitutes the segment between Iceland and the Faroe Islands, with a maximum sill depth of about 500 m (Figure 1).

The complex interaction of warm and saline Atlantic-origin Waters flowing northward with cold and fresh Polar Water flowing southward is strongly influenced by the presence of the GSR. As such, the GSR does not only limit the flow of dense-water from the Nordic Seas into the subpolar North Atlantic, but also significantly impacts heat and freshwater distributions, the location of convection sites, and ultimately the stability of the AMOC. Understanding these dynamics is essential for predicting the response of high-latitude ocean systems to ongoing climate change (Brakstad et al., 2023; Chafik & Rossby, 2019; Drijfhout et al., 2012; Lozier et al., 2019; Meehl et al., 2014; Tsubouchi et al., 2021; Winton et al., 2013).

The IFR is a crucial segment of this system. The ridge facilitates complex exchanges of water masses: at the surface, warm Atlantic water flows northward, and at depth, cold and dense Arctic-origin water flows southward atop and around the ridge, including through the FBC (Bacon et al., 2022; de Marez et al., 2024). Past studies using glider observations proposed that there exists a pathway connecting the surface and the bottom waters near

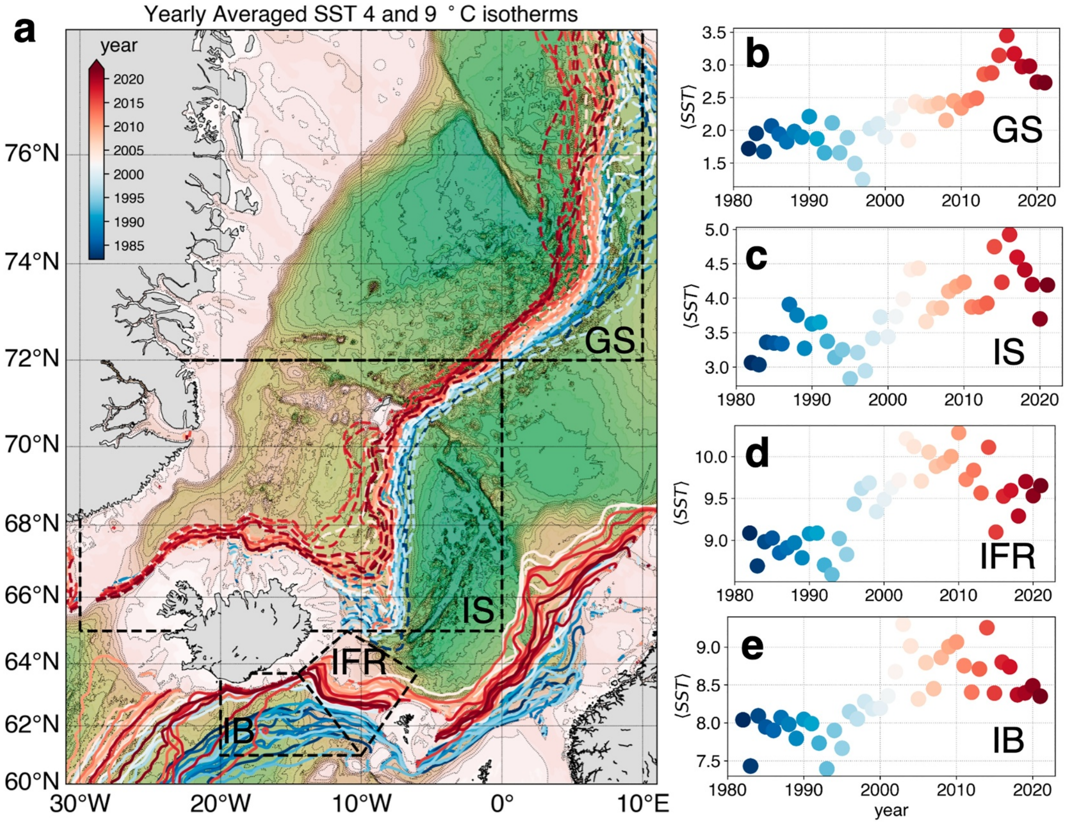

Figure 1. (a), Temporal evolution of the 4°C (dashed line) and 9°C (solid line) surface isotherms from yearly averages over the period 1981–2022. (b, c, d and e), Yearly averaged sea surface temperature evolution in the Greenland Sea (GS), Iceland Sea (IS), Iceland-Faroe Ridge (IFR), and Iceland Basin (IB), respectively (definition of these areas is indicated by dashed boxes in panel a).

the IFR. For example, Beaird et al. (2016) suggested that the vertical transfers are mainly due to winter convection, mixed layer instability, and deep frontal subduction. At the same time, it was shown that the ridge supports the formation of mesoscale eddies (Guo et al., 2014), which could play a pivotal role in the vertical redistribution of heat and other tracers. The lack of resolution of current altimetry and numerical models, however, hindered a comprehensive analysis of the mesoscale activity near the IFR. Therefore, many questions regarding the mechanisms by which mesoscale dynamics atop the ridge influence vertical heat fluxes remain. We consider this latter mechanism a key component that could significantly modulate ocean-atmosphere interactions in the area.

This study is timely due to the recent warming of surface waters in the region: along with the rest of the global ocean, the surface waters of the northeastern part of the North Atlantic have been observed to warm in recent decades (Polyakov et al., 2017; Shi et al., 2024). These waters are warming up to twice as fast as the global average (Pörtner et al., 2019). Specifically south of Iceland, it is striking that the 9°C annual mean isotherm has shifted northwards to the IFR. In this region, surface waters have become significantly warmer, increasing by about 1°C over the past 40 years (Figure 1). Rising sea surface temperatures can amplify stratification and alter mesoscale eddy activity, potentially reshaping the dynamics governing vertical heat fluxes. Given the critical role of the IFR region in ocean circulation and climate regulation, it is imperative to assess how these ongoing changes impact heat transfer processes. This study addresses this pressing need by providing new insights into mesoscale eddy dynamics using newly released high-resolution altimetry and numerical modeling. We discuss the influence of the mesoscale dynamics on vertical heat fluxes, thereby advancing our understanding of the evolving physical oceanography of the Iceland-Faroe Ridge.

2. Data and Methods

2.1. SWOT Data

We leverage newly released satellite data from the Surface Water and Ocean Topography (SWOT) satellite, a collaborative effort between NASA and CNES launched in late 2022, to unveil unprecedented details of surface mesoscale geostrophic turbulence over the IFR (Morrow et al., 2019). Specifically, we use the SWOT_L3_SSH product, derived from the L2 SWOT KaRIn Low rate ocean data products provided by NASA/JPL and CNES. This data set is produced and freely distributed by the AVISO and DUACS teams as part of the DESMOS Science Team project (AVISO/DUACS, 2023). The Sea Level Anomaly (SLA) is displayed on a 2-km resolution grid. We use the "denoised" SLA for our analysis (Figure 2c), which is produced using an AI-based noise-mitigation algorithm as described in Dibarboure et al. (2023, 2025). Note that this procedure smoothens SSH gradients, and therefore reduces the energy of the signal. However, using this version of SLA allows the computation of instantaneous geostrophic velocities (u_{swot}, see Figure 2d) and normalized relative vorticity (ζ/f, Figure 2e) at unprecedented resolution. The two-dimensional data provided by SWOT, without further interpolation, offers a more accurate estimate of the horizontal structure of surface ocean currents for the first time. Recent studies (Carli et al., 2025; Damerell et al., 2025; Du & Jing, 2024; Tchilibou et al., 2025; Verger-Miralles et al., 2024; Wang et al., 2025; X. Zhang et al., 2024; Z. Zhang et al., 2024) unveiled the SWOT's ability to resolve small eddies, revealing structures of smaller extent than those detected in gridded altimetric products (using a detection algorithm, here *py-eddy-tracker,* Mason et al., 2014). As an example, the SLA from SWOT is compared with SLA data from a 1/8° gridded product provided by AVISO on the same day (Figure 2b).

We use data from the 1-day repeat orbit phase spanning the period 03/29/2023–07/08/2023 to compute the average Eddy Kinetic Energy $\langle EKE\rangle$. This is calculated as $\langle EKE\rangle = \langle \frac{1}{2}\left({u'_{\text{swot}}}^2 + {v'_{\text{swot}}}^2\right)\rangle$, where $u'_{\text{swot}} = u_{\text{swot}} - \langle u_{\text{swot}}\rangle$, with u and v being the instantaneous velocities and $\langle\cdot\rangle$ denoting a temporal average over the entire period. This allows for the first time to provide a synoptic estimate of the mesoscale activity on the IFR.

2.2. GIGATL1 Simulation

We use outputs from a realistic numerical simulation conducted as part of the GIGATL set of Atlantic Ocean simulations (Gula et al., 2021), using the Coastal and Regional Ocean COmmunity model (CROCO), a version of the ROMS model (Shchepetkin & McWilliams, 2005). This model solves the hydrostatic primitive equations using the full equation of state for seawater (Shchepetkin & McWilliams, 2011). Specifically, we use the GIGATL1 version with a horizontal resolution of 1 km and 100 terrain-following levels, which allows resolution of mesoscale dynamics on the IFR. The simulation is initialized in July 2007 using outputs from the GIGATL3 simulation, which has a 3 km horizontal resolution and is initialized with the Simple Ocean Data Assimilation (SODA) (Carton & Giese, 2008) and spun up for 3 years. Boundary conditions are provided by SODA, while the simulation is forced with hourly atmospheric forcing from the Climate Forecast System Reanalysis (CFSR) (Saha et al., 2010), using a bulk formulation with relative winds (Renault et al., 2020). Tidal effects are included, with barotropic tidal forcing at the boundaries and tidal potential and self-attraction taken from TPXO7.2 (Egbert & Erofeeva, 2002) and GOT99.2b (Ray, 1999), respectively. Bathymetry data are obtained from the SRTM30plus data set (Becker et al., 2009). The k-ϵ turbulence closure scheme is used for vertical mixing parameterization, with the Canuto A stability function formulation applied (Canuto et al., 2001). No explicit lateral diffusivity is included in the simulation. Bottom friction effects are parameterized using a logarithmic law of the wall with a roughness length of 0.01 m. For this study, we use daily averages to remove the tidal signature, covering a 1-year period to capture a full seasonal cycle. Quantities averaged over this seasonal cycle are denoted as $\langle\cdot\rangle$. The EKE from GIGATL1 output is computed using the same definition as for the SWOT data. Previous studies leveraging the GIGATL ensemble have discussed and validated these simulations extensively (Barkan et al., 2021; Mashayek et al., 2021; Napolitano et al., 2024; Qu et al., 2021; Ruan et al., 2021; Schubert et al., 2023; Tagliabue et al., 2022; Uchida et al., 2022; Vic et al., 2022).

From the GIGATL1 outputs, the turbulent vertical kinematic heat flux (VHF $= C_{\text{p}}\rho_0 w'T'$, see, e.g., McPhee, 1992; McPhee & Martinson, 1994; Su et al., 2018) is computed along designated vertical sections. C_{p} is the specific heat capacity of sea water and ρ_0 is the average density of sea water. The vertical velocity w and temperature T are low-pass filtered to remove the influence of internal waves. The filter is a 4th-order Butterworth filter with a cutoff frequency of 1 week. Then, anomalies are computed as $w' = w^* - \langle w\rangle_{\text{month}}$ and

$T' = T^* - \langle T \rangle_{\text{month}}$, where $\cdot^*$ denotes the filtered quantities, and $\langle \cdot \rangle_{\text{month}}$ are monthly averages. This procedure ensures that only the influence of mesoscale structures is considered, and takes into account the seasonal variations of temperature on the vertical.

To study the nature of the instabilities responsible for the generation of mesoscale structures on the IFR, we compute energy transfers from the GIGATL1 outputs in the same fashion as in, for example, Gula et al. (2016). Assuming that the flow can be decomposed as $\boldsymbol{u} = \langle \boldsymbol{u} \rangle_{\text{month}} + \boldsymbol{u}'$, the transfer from the Mean Kinetic Energy (MKE) to the kinetic energy of the perturbation (the EKE) can be expressed as:

$$\mathcal{T}_{\text{MKE}\to\text{EKE}} = HRS + VRS, \tag{1}$$

where

$$HRS = -\langle u'^2 \rangle \partial_x \langle u \rangle - \langle u'v' \rangle \partial_y \langle u \rangle - \langle v'^2 \rangle \partial_y \langle v \rangle - \langle u'v' \rangle \partial_x \langle v \rangle, \tag{2}$$

is the contribution from the Horizontal Reynolds Stress (the subscript $\cdot_{\text{month}}$ has been omitted for simplicity here), and

$$VRS = -\langle u'w' \rangle \partial_z \langle u \rangle - \langle v'w' \rangle \partial_z \langle v \rangle, \tag{3}$$

is the contribution of the Vertical Reynolds Stress. Second, the transfer from the Potential Energy (PE) of the perturbation to the EKE is the Vertical Buoyancy Flux:

$$\mathcal{T}_{\text{PE}\to\text{EKE}} = VBF = \langle w'b' \rangle. \tag{4}$$

The transfer terms shown in Figures 2i and 2j are then averaged over a full seasonal cycle and integrated vertically.

Finally, we conduct offline 3D particle advection simulations using the Python code *Pyticles*, which is specifically designed for CROCO model outputs. The source code and a comprehensive list of studies using this tool are available at https://github.com/Mesharou/Pyticles. In these simulations, particles are initially seeded within a 500 × 500 km box centered at 63.5°N, 11°W, with 10 km spacing on the 80th and 90th vertical levels (close to the surface). The advection simulation we show spans 5 months, starting in November, with particles continuously injected each month, resulting in a total of 24,670 particles. Additional simulations with different seeding periods were conducted (not shown here) and showed no conceptual differences from the results presented in this study.

2.3. In Situ Measurements Around Iceland

The Sea Surface Temperature (SST) measurements shown in Figure 1 are from NOAA/NCEI 1/4° Daily Optimum Interpolation Sea Surface Temperature (OISST), Version 2.1 (Banzon et al., 2014).

The ocean current velocity data shown in Figure 4c were collected during the 2021 NORSE pilot cruise aboard the R/V Armstrong. The plot shows the combined shipboard ADCP WH300 and OS38 kHz. The derived velocities are obtained using the UHDAS toolbox (Firing & Hummon, 2010).

We use in situ temperature and salinity (T/S) data in the period 1980–2020, part of the SDC_ARC_DATA_TS_V2 Nordic Seas data set published at the Norwegian Marine Data Center (Brakstad, Ailin and Våge, Kjetil and Ólafsdóttir, Sólveig Rósa and Jeansson, Emil and Gebbie, Geoffrey, 2023). We also included data from the Argo float program (Wong et al., 2020) in the area of interest in the period 2000–2020. The total number of data points used for the histograms shown in Figure 5 are 118,847, 40,908, and 73,989, in the range $1 < \text{CT} < 6$°C and $35 < \text{SA} < 35.4$ g kg^{-1}. The profiles used cover the area along the Icelandic shelf with 61 °N constituting the southern boundary (see Figure 1).

3. Results

3.1. Unveiling the Mesoscale Turbulence on Top of the IFR

Novel high-resolution satellite altimetry data reveal the presence of highly turbulent flow characterized by numerous mesoscale structures atop the IFR (see bathymetric map of the area in Figure 2a). The relatively small horizontal size of mesoscale eddies in this region, determined by the first baroclinic Rossby deformation radius being in the order of 10 km (Chelton et al., 1998), has previously hindered the detailed analysis of mesoscale activity. For example, eddies detected on the IFR in classical gridded-altimetry products (Figure 2b) have diameters of $\mathcal{O}$(100 km).

However, the reality differs significantly: the SLA measurements from SWOT altimetry on the same day reveal unprecedented details of the SLA field (Figure 2c) and demonstrate that classical altimetry misrepresents eddies in this region. A striking example is the cyclonic eddy located near ~12°W, 63.3°N, which is 2–3 times smaller in the SWOT observation than in the AVISO product. The same applies to the cyclonic eddy further north near ~12°W, 64.5°N. Another example is a small cyclone located near ~10°W, 62.5°N, only seen in SWOT data and not visible in the AVISO product.

The noise-reduced SWOT data enables the computation of geostrophic currents (Figure 2d) and relative vorticity (Figure 2e). The latter highlights the numerous mesoscale eddies with a radius in the order of the Rossby deformation radius $\mathcal{O}$(10 km), previously unobservable with classical altimetry, but now captured synoptically by SWOT. These eddies are responsible for an intense turbulent flow over the IFR. This turbulence is concentrated on the IFR, as indicated by higher values of mean EKE over the IFR compared to regions over the basin interior outside topographic slopes (Figure 2f).

A high-resolution, realistic numerical simulation further enables a comprehensive study of this mesoscale turbulence. The GIGATL1 simulation reproduces the turbulence observed with SWOT with remarkable accuracy both in terms of relative vorticity (Figures 2e and 2g) and EKE (Figures 2f and 2h). The diameters of the eddies, represented by patches of relative vorticity, are comparable in SWOT and GIGATL1. The smaller absolute values of relative vorticity ζ/f in the SWOT derived data compared to the GIGATL1 output can mainly be attributed to the noise-removing processing step for the SWOT data. High values of EKE are concentrated around similar locations in SWOT and GIGATL1, with even the order of magnitude of EKE being comparable. Note that although the SWOT data analyzed here covers only the spring–summer 2023 period, both the extended 2024 SWOT observations and the GIGATL1 simulation confirm that intense mesoscale activity over the IFR persists year-round, with model-based EKE peaking outside the SWOT period (not shown).

The GIGATL1 simulation also provides access to 3D fields and facilitates advanced diagnostics such as energy transfer terms (see Methods, Section 2.2). These terms are, on average, positive at the position of a jet located in the Western Valley of the IFR (see Figures 2i and 2j and Hansen et al., 2023). The observed mesoscale eddies thus originate from barotropic and baroclinic instabilities of this jet, which effectively acts as an "eddy shotgun." This can be noticed, for example, in the relative vorticity field (Figure 2g). The eddies subsequently propagate southeastward along the ridge, driven by topographic Rossby waves (de Marez et al., 2017), populating the IFR with coherent structures. As they follow the ridge, some eddies eventually cross it, populating the southern flank with coherent structures.

3.2. Impact of the Mesoscale Turbulence on Vertical Motions

The high-resolution realistic numerical simulation unveils the impact of mesoscale turbulence on the vertical transport of tracers—particularly temperature—from the surface down to the bottom layer. This vertical transport can be qualitatively illustrated by seeding particles in the simulation at the surface and running 3D particle advection schemes (see Methods, Section 2). We extract the particles that were seeded in the open ocean (excluding those from the continental shelf) and completed their journeys south of the IFR at depths below 500 m. The points in the scatter plots of Figure 3 correspond to the cumulative section of the positions of all these specific particles at all timesteps of the simulations. We estimate the EKE and the normalized relative vorticity of the particles by extracting the values from the GIGATL1 outputs at the corresponding grid points. The analysis reveals that when seeded at the surface, the particles reaching the ocean bottom south of the IFR experience high EKE values along their paths (Figure 3a). Most of the particles sink near the IFR, at a distance between 200 and 400 km south of its shallowest part (Figure 3b). They also encounter high values of relative vorticity (Figures 3c

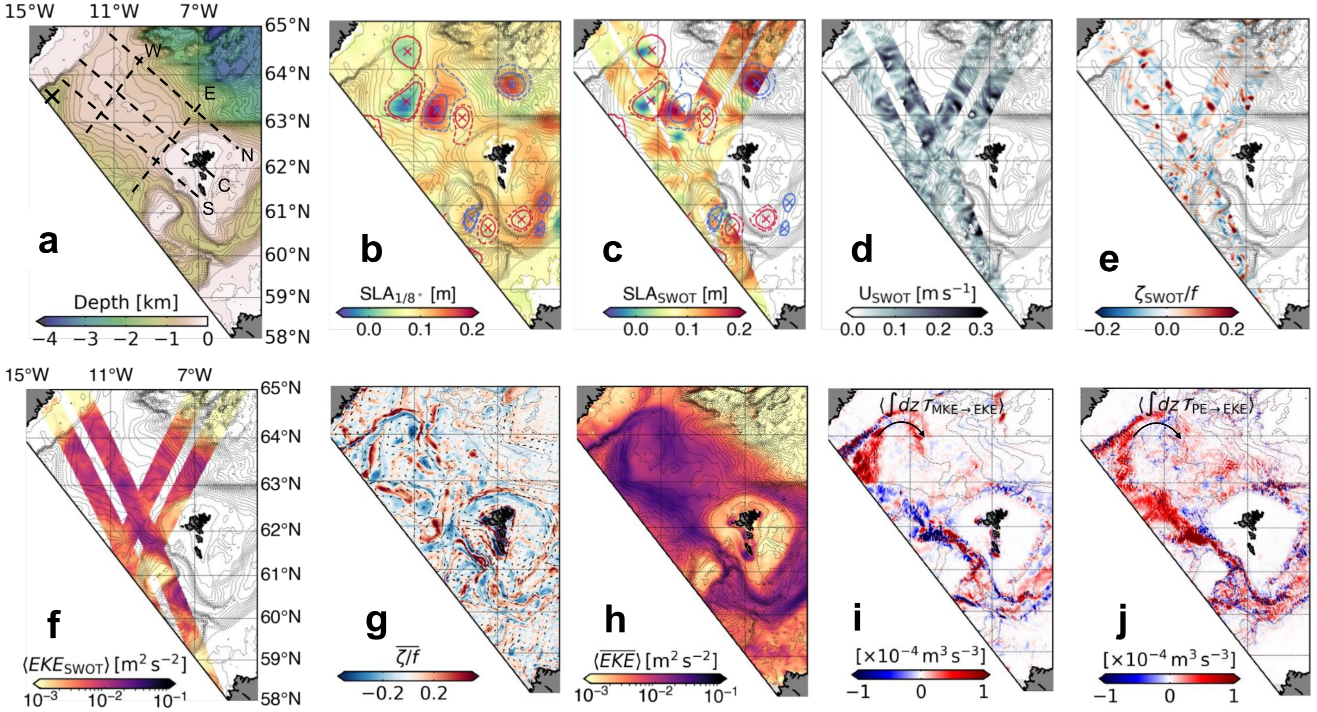

Figure 2. (a), Bathymetric map of the IFR area. (b), Snapshot of SLA from 1/8° gridded altimetry on 06/10/2023, and contours of cyclonic (red) and anticyclonic (blue) mesoscale eddies using the *py-eddy-tracker* algorithm. (c), SWOT KaRIn 2-km resolution noiseless SLA in passes #5 and #16 on 06/10/2023; the eddy detection from the gridded product is superimposed. (d), Geostrophic velocity magnitude derived from SWOT SLA. (e), Normalized relative vorticity estimated from SWOT-derived geostrophic currents. (f), Eddy Kinetic Energy estimated from SWOT-derived geostrophic currents, averaged over the period 03/29/2023–07/08/2023. (g), Normalized relative vorticity, averaged vertically, estimated from GIGATL1 outputs, on 06/25/2008 —note the different color range in (d and f. h), Eddy Kinetic Energy estimated from GIGATL1 simulation outputs, averaged vertically and over one seasonal cycle. (i, j), Average energy transfer terms in GIGATL1 outputs. The arrow marks the jet location in the Western Valley that generates eddies through instabilities, which is referred to as “eddy shotgun” in the manuscript.

and 3d). This shows that sinking water parcels south of the IFR are likely influenced by mesoscale turbulence during their descent.

More specifically, diagnostics from GIGATL1 show that mesoscale turbulence induces vertical fluxes of temperature from the surface down to the bottom layer. The turbulent vertical kinematic heat flux (or Vertical Heat Flux, VHF $= C_p \rho_0 w'T'$, see Methods, Section 2) generated by individual mesoscale events reaches magnitudes exceeding 10^3 W m^{-2}. As a first example, the bottom-reaching jet located in the Western Valley of the IFR which often deflects eastward to form an anticyclonic gyre, produces intense VHF from the surface to the seafloor (Figures 4a and 4c). As a second example, coherent surface-intensified eddies, formed remotely by the eddy shotgun, extend down to the bottom layer. The VHF associated with these eddies is observed to penetrate the $\sigma_0 = 27.8$ kg m^{-3} isopycnal (Figure 4b).

Therefore, quantitatively, there is an intense eddy-driven transfer of heat toward the bottom atop the IFR. On average, the VHF over the IFR displays a clear pathway from the surface to the bottom, with a magnitude of $\mathcal{O}(10^2$ W m$^{-2})$ (Figures 4d and 4e). These values are consistent with in situ observations (Thompson et al., 2016) and estimates from other high-resolution numerical simulation analyses (Su et al., 2018). They are 10 times larger than the mesoscale vertical heat transport observed in most regions of the ocean (Su et al., 2018), comparable in magnitude to air-sea heat fluxes (Large & Yeager, 2009), and persist throughout the entire seasonal cycle. This highlights the predominance of eddy-induced heat flux compared to convection-induced heat flux, which occurs only during winter (Su et al., 2018). Peak values exceeding 10^3 W m^{-2} are observed at two major vertical heat transfer hotspots: one located on the western side of the ridge and the other on the eastern side, where remotely generated eddies accumulate (Figures 2g, 2h and 4f).

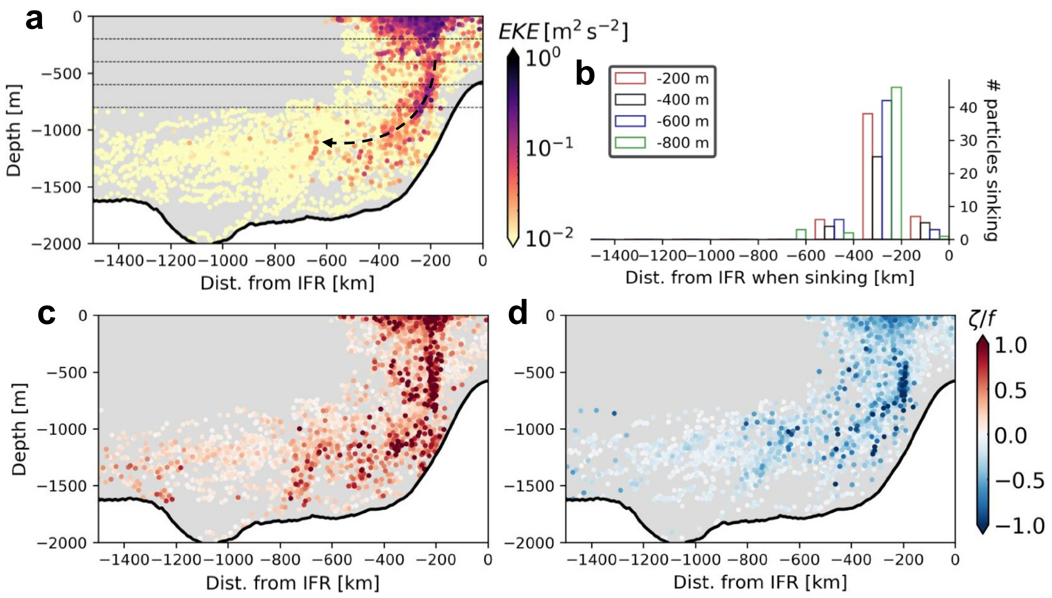

Figure 3. (a), Across-ridge cumulative section of EKE of particles advected in GIGATL1 outputs; the position of particles is presented as their depth versus their distance from the IFR (with negative value meaning south of the IFR); the bold line shows the along-slope averaged topography. (b), Histogram showing the distance from the IFR at which particles sank below 4 selected depths: 200,400, 600 and 800 m, shown by the dashed lines in panel a. (c, d), Same as panel a but for normalized particle relative vorticity (c, positive, d, negative).

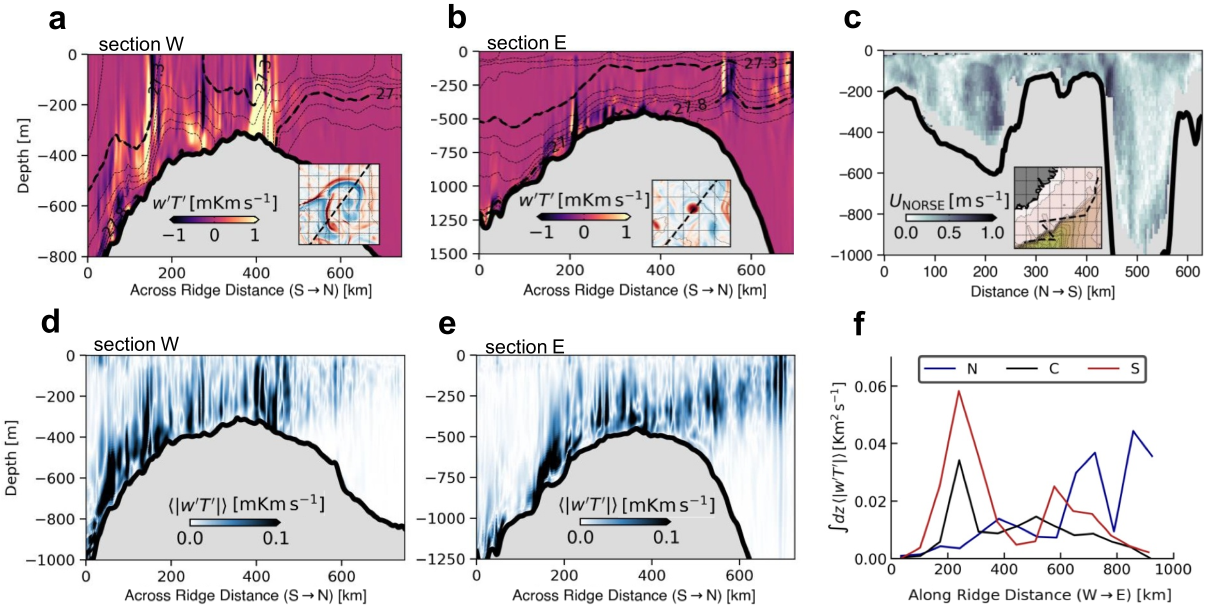

Figure 4. (a), Snapshot of $w'T'$ along the section labeled W in Figure 2a, from south to north; the dashed lines show isopycnals with a 0.1 kg m^{-3} spacing; the inset shows the surface relative vorticity at the time of the section, with the same colormap as in Figure 2e and the position of the section. (b), Same as panel a along the section labeled E in Figure 2a. (c), Along track section of the current speed from the NORSE cruise over the IFR's Western Valley; the inset shows the bathymetry and the pathway of the vessel. (d), (resp. e) $\langle|w'T'|\rangle$ (averaged over 1 year of simulation) along the section labeled E (resp. W) in panel b. (f), Vertically integrated average Vertical Heat Flux magnitude along the sections labeled N, C, and S in Figure 2a.

This intense VHF is also evident at the ocean floor, where currents flow along the topography (see Figure S1 in Supporting Information S1). In particular, on the southern flank of the IFR, a bottom current, described by Perkins et al. (1998), Olsen et al. (2016) and more recently by de Marez et al. (2024), generates bottom-intensified vortices through intrinsic barotropic and baroclinic instabilities (Guo et al., 2014). These vortices produce bottom-intensified VHF, which thickens the bottom mixed layer connecting the seafloor with the ocean interior, similar to what has been observed in past in situ measurements (de Marez et al., 2024; Fer et al., 2010).

4. Discussion on the Fate of ISOW

Dense waters formed in the Nordic Seas may flow across the GSR into the subpolar North Atlantic as overflow waters (Bacon et al., 2022). The portion of overflow water that leaves through FBC or across the IFR is referred to as ISOW (Johns et al., 2021; Kanzow & Zenk, 2014; Zou et al., 2017, 2020). As a bottom-intensified current, ISOW flows along the southern slope of the IFR (de Marez et al., 2024) and eventually around the Reykjanes Ridge, doubling its volume along the pathway due to entrainment (Johns et al., 2021). ISOW constitutes about 1/3 of the total overflow that feeds into the lower limb of the AMOC and is thus an important contributor (Devana & Johns, 2024). It is typically defined as the water mass below the $\sigma_0 = 27.8$ kg m^{-3} isopycnal (see all literature on ISOW characterization since Bowles & Jahn, 1983). This water mass used to have a clear —historical— T/S signature (Saunders, 1996, and Figure 5a), which can be observed far downstream throughout the subpolar gyre (Van Aken & Becker, 1996). Modification of ISOW by entrainment has thus significant impacts on the hydrographic signature of the lower limb of the AMOC.

A compilation of all available data collected where the ISOW flows south of Iceland, in the Iceland Basin (IB, see Figure 1a), provides compelling evidence of significant changes over the past 40 years, with a temperature increase of approximately ~ 0.5°C (Figures 5b and 5c). This is consistent with the observed warming of bottom temperatures in the FBC, monitored by a mooring array and quantified at 0.1°C per decade by Larsen et al. (2024). The mechanisms potentially responsible for the ISOW warming are limited and can be narrowed down to two main processes.

First, assuming no mixing with ambient water during its transit, the T/S properties of ISOW should remain unchanged between its formation site (major contribution from the Greenland Sea (GS), see Brakstad et al., 2023) and the measurement site, here the IB. In the GS, profound changes in surface temperatures are occurring (see Figure 1 and Figure S2 in Supporting Information S1). This suggests that the first plausible cause of ISOW warming south of Iceland originates in the far-field, by the warming of the source of ISOW, the surface waters of the GS, see Figures S2e and S2f in Supporting Information S1. This hypothesis aligns with findings from Strehl et al. (2024), who documented the warming of deep water formed in the GS, and with the conclusions of Larsen et al. (2024), who recently proposed that the warming of overflow bottom water observed in the FBC originates further north of the IFR.

Second, as ISOW flows from its generation site to the North Atlantic, the IFR is the only location where it is sufficiently close to surface waters (Beaird et al., 2016) to be influenced by surface warming at a location other than its formation site (Figure 1). At this critical location, our study highlights strong mesoscale turbulence-induced VHF $\mathcal{O}\left(10^2 \text{ W m}^{-2}\right)$, revealed through both SWOT altimetry and high-resolution numerical simulations. This turbulence creates a direct pathway between the warming surface waters (Figure 1) and the ISOW layer (Figure 4). This observation aligns with previous glider data suggesting subduction of the Iceland-Faroe Front atop the IFR (Beaird et al., 2016). We show here that the mesoscale turbulence is likely facilitating this subduction. While the diagnosed eddy-induced VHF over the IFR are strong, they represent local and episodic maxima. For comparison, a 0.1°C per decade warming of the ISOW layer (~500–1,000 m thick) corresponds to a net heat input of only $\mathcal{O}\left(1 \text{ W m}^{-2}\right)$. This suggests that eddy-induced VHF has the potential to contribute significantly to ISOW warming, but likely acts in conjunction with far-field changes in source-water properties. Also, we note that other near-field processes, such as local mixing of upper-layer waters into the overflow layer as it crosses the IFR or after excitement of internal waves, may also contribute to ISOW warming in this region, independently of eddy activity.

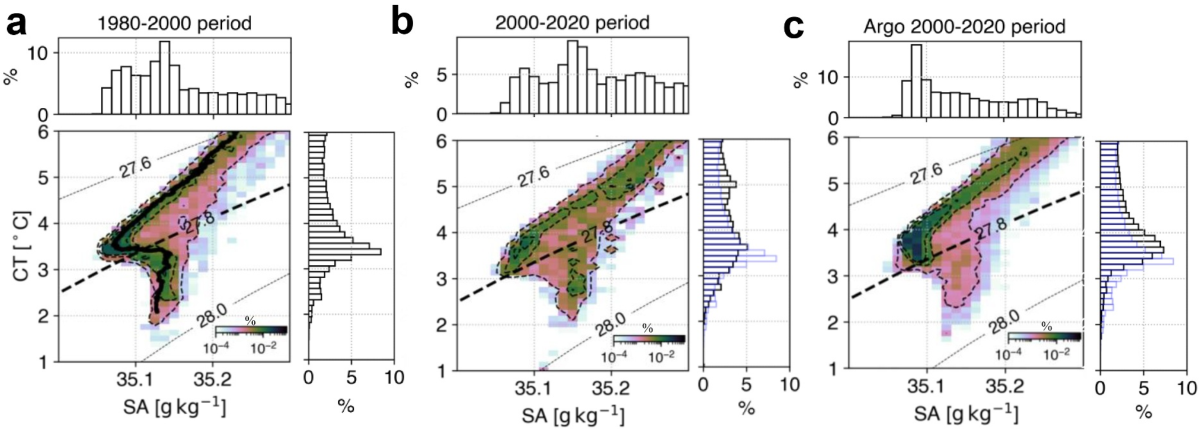

Figure 5. (a) (resp. b), TS diagrams from shipboard hydrographic Conservative Temperature CT and Absolute Salinity SA data over the period 1980–2000 (resp. 2000–2020) in the Iceland Basin (IB area in Figure 1a); they are shown as 2D histograms with the color representing the percentage of datapoints relative to the total of points in the TS diagram; black line in a shows a particular cast from Saunders (1996) presenting the historical "chair-like" profile of the ISOW; insets show cumulative histograms over salinity and temperature axes. (c), same as a, b from Argo floats data in the same area for the period 2000–2020. Blue bars plots in inserts of panels b, c recall the cumulative histogram for temperature in the period 1980–2000.

5. Conclusion

The observed temperature increase over the past 40 years, together with IPCC projections (Pörtner et al., 2019), suggests that bottom water temperatures could rise by 1–3°C by the end of the century. The current lack of comprehensive in situ data and time coverage in high-resolution numerical simulations constrain our ability to provide stronger evidence for the mechanisms driving this warming. Our study identifies eddy-induced vertical heat fluxes as a key mechanism that may explain local hotspots of bottom-water warming, potentially occurring in other regions with similar topography. This mechanism may lead to an acceleration of the bottom-water warming due to enhanced mesoscale activity at a global scale (Barceló-Llull et al., 2024; Beech et al., 2022; Martínez-Moreno et al., 2021). We thus emphasize the need for timely monitoring of changes in bottom-water properties as these will impact benthic species populations and the global ocean circulation.

Data Availability Statement

SWOT data and gridded-altimetry data can be downloaded on AVISO website https://www.aviso.altimetry.fr/en/my-aviso-plus.html. *in situ data* are provided by the SeaDataNet Pan-European infrastructure for ocean and marine data management (https://www.seadatanet.org), and can be downloaded as part of the SDC_ARC_DATA_TS_V2 data set and the Norwegian Marine Data Center (Brakstad, Ailin and Våge, Kjetil and Ólafsdóttir, Sólveig Rósa and Jeansson, Emil and Gebbie, Geoffrey, 2023). Due to the large size of simulation outputs from GIGATL1, they are available upon request. Historical data from Saunders (1996) are accessible via the MEDIN portal (https://portal.medin.org.uk), which collects marine data across UK organisations. The Argo floats data are available on the Ifremer portal (https://data-argo.ifremer.fr/dac/). Satellite measurements of temperature can be downloaded using NOAA download services at https://www.ncei.noaa.gov/data/sea-surface-temperature-optimum-interpolation/. The ocean current velocity data were collected during the 2021 NORSE pilot cruise aboard the R/V Armstrong, and they are available following UCSD's portal http://www.mod.ucsd.edu/norse.

Acknowledgments
C.d.M. was supported by a Queen Margrethe II's and Vigdís Finnbogadóttir's Interdisciplinary Research Centre on Ocean, Climate and Society (ROCS) postdoctoral fellowship. A.R.A. was supported by ROCS. J.G. was supported by the French National Agency for Research (ANR) through the project DEEPER (ANR-19-CE01-0002-01). GIGATL simulations were performed using HPC resources from GENCI-TGCC (Grants 2024-A0170112051). Particle advection simulations were performed using the HPC facilities DATARMOR of "Pôle de Calcul Intensif pour la Mer" at Ifremer, Brest, France. We would like to acknowledge the significant effort invested in acquiring and maintaining the Hydrography Observational Programme by the Icelandic Marine and Freshwater Research Institute. Additional computer resources and research IT are provided by UTS of the University of Iceland through the Icelandic research e-Infrastructure project (IREI), funded by the Icelandic Infrastructure Fund. A.R.A. is grateful to the organizers of the OCB–US CLIVAR joint workshop, "Pathways Connecting Climate Changes to the Deep Ocean: Tracing Physical, Biogeochemical, and Ecological Signals from the Surface to the Deep Sea," which highlighted broader applications of this work. We thank the reviewers for their insightful comments that greatly improved the manuscript quality.

References

AVISO/DUACS. (2023). SWOT Level-3 SSH basic (v0.3) [Dataset]. https://doi.org/10.24400/527896/A01-2023.017

Bacon, S., Garabato, A. C. N., Aksenov, Y., Brown, N. J., & Tsubouchi, T. (2022). Arctic Ocean boundary exchanges. *Oceanography*, *35*(3/4), 94–102.

Banzon, V. F., Reynolds, R. W., Stokes, D., & Xue, Y. (2014). A 1/4-spatial-resolution daily sea surface temperature climatology based on a blended satellite and in situ analysis. *Journal of Climate*, *27*(21), 8221–8228. https://doi.org/10.1175/jcli-d-14-00293.1

Barceló-Llull, B., Rosselló, P., Combes, V., Sánchez-Román, A., Pujol, M. I., & Pascual, A. (2024). Robust intensification of global ocean Eddy Kinetic Energy from three decades of satellite altimetry observations. *arXiv preprint arXiv:2406.08014*. https://doi.org/10.48550/arXiv.2406.08014

Barkan, R., Srinivasan, K., Yang, L., McWilliams, J. C., Gula, J., & Vic, C. (2021). Oceanic mesoscale eddy depletion catalyzed by internal waves. *Geophysical Research Letters*, *48*(18), e2021GL094376. https://doi.org/10.1029/2021gl094376

Beaird, N., Rhines, P., & Eriksen, C. (2016). Observations of seasonal subduction at the Iceland-Faroe front. *Journal of Geophysical Research: Oceans*, *121*(6), 4026–4040. https://doi.org/10.1002/2015jc011501

Becker, J. J., Sandwell, D. T., Smith, W. H. F., Braud, J., Binder, B., Depner, J., et al. (2009). Global bathymetry and elevation data at 30 Arc seconds resolution: SRTM30_plus. *Marine Geodesy*, *32*(4), 355–371. https://doi.org/10.1080/01490410903297766

Beech, N., Rackow, T., Semmler, T., Danilov, S., Wang, Q., & Jung, T. (2022). Long-term evolution of ocean eddy activity in a warming world. *Nature Climate Change*, *12*(10), 910–917. https://doi.org/10.1038/s41558-022-01478-3

Blindheim, J. (1990). Arctic intermediate water in the Norwegian Sea. *Deep-Sea Research, Part A: Oceanographic Research Papers*, *37*(9), 1475–1489. https://doi.org/10.1016/0198-0149(90)90138-l

Bowles, F. A., & Jahn, W. H. (1983). Geological/geophysical observations and inferred bottom-current flow: South flank Iceland—Faeroe Ridge. *Marine Geology*, *52*(3–4), 159–185. https://doi.org/10.1016/0025-3227(83)90054-3

Brakstad, A., Gebbie, G., Våge, K., Jeansson, E., & Ólafsdóttir, S. R. (2023a). Formation and pathways of dense water in the Nordic Seas based on a regional inversion. *Progress in Oceanography*, *212*, 102981. https://doi.org/10.1016/j.pocean.2023.102981

Brakstad, A., Våge, K., Ólafsdóttir, S. R., Jeansson, E., & Gebbie, G. (2023b). Hydrographic and geochemical observations in the nordic seas between 1950 and 2019, 102981. https://doi.org/10.21335/NMDC-1271328906

Canuto, V. M., Howard, A., Cheng, Y., & Dubovikov, M. (2001). Ocean turbulence. Part I: One-Point closure model—Momentum and heat vertical diffusivities. *Journal of Physical Oceanography*, *31*(6), 1413–1426. https://doi.org/10.1175/1520-0485(2001)031<1413:otpiop>2.0.co;2

Carli, E., Tranchant, Y., Siegelman, L., Le Guillou, F., Morrow, R. A., Ballarotta, M., & Vergara, O. (2025). *Small-scale eddy diagnostics around the southern ocean polar Front with SWOT*. Authorea Preprints.

Carton, J. A., & Giese, B. S. (2008). A reanalysis of ocean climate using Simple Ocean Data Assimilation (SODA). *Monthly Weather Review*, *136*(8), 2999–3017. https://doi.org/10.1175/2007MWR1978.1

Chafik, L., & Rossby, T. (2019). Volume, heat, and freshwater divergences in the subpolar North Atlantic suggest the Nordic Seas as key to the state of the meridional overturning circulation. *Geophysical Research Letters*, *46*(9), 4799–4808. https://doi.org/10.1029/2019gl082110

Chelton, D. B., de Szoeke, R. A., Schlax, M. G., El Naggar, K., & Siwertz, N. (1998). Geographical variability of the first Baroclinic Rossby radius of deformation. *Journal of Physical Oceanography*, *28*(3), 433–460. https://doi.org/10.1175/1520-0485(1998)028⟨0433:GVOTFB⟩2.0.CO;2

Damerell, G. M., Bosse, A., & Fer, I. (2025). Merging of a mesoscale eddy into the Lofoten Vortex in the Norwegian Sea captured by an ocean glider and SWOT observations. *EGUsphere*, *2025*, 1–28.

de Marez, C., Carton, X., Morvan, M., & Reinaud, J. N. (2017). The interaction of two surface vortices near a topographic slope in a stratified ocean. *Fluids*, *2*(4), 57. https://doi.org/10.3390/fluids2040057

de Marez, C., Ruiz-Angulo, A., & Le Corre, M. (2024). Structure of the bottom boundary current South of Iceland and spreading of deep waters by submesoscale processes. *Geophysical Research Letters*, *51*(5), e2023GL107508. https://doi.org/10.1029/2023gl107508

Devana, M., & Johns, W. (2024). Structure and variability of Iceland Scotland overflow water transport in the western Iceland basin. *Journal of Geophysical Research: Oceans*, *129*(8), e2023JC020107. https://doi.org/10.1029/2023jc020107

Dibarboure, G., Faugere, Y., Delepoulle, A., Briol, F., Raynal, M., Ubelmann, C., et al. (2023). SWOT Level-3 Overview algorithms and examples. Retrieved From https://swotst.aviso.altimetry.fr/fileadmin/user_upload/SWOTST2023/postersPI/faugere_ocean_l3_PIproject.pdf. (Poster at SWOT Science Team 2023

Dibarboure, G., Anadon, C., Briol, F., Cadier, E., Chevrier, R., Delepoulle, A., et al. (2025). Blending 2D topography images from the Surface Water and Ocean Topography (SWOT) mission into the altimeter constellation with the level-3 multi-mission Data Unification and Altimeter Combination System (DUACS). *Ocean Science*, *21*(1), 283–323. https://doi.org/10.5194/os-21-283-2025

Drijfhout, S., Van Oldenborgh, G. J., & Cimatoribus, A. (2012). Is a decline of AMOC causing the warming hole above the North Atlantic in observed and modeled warming patterns? *Journal of Climate*, *25*(24), 8373–8379. https://doi.org/10.1175/jcli-d-12-00490.1

Du, T., & Jing, Z. (2024). Fine-scale eddies detected by SWOT in the Kuroshio extension. *Remote Sensing*, *16*(18), 3488. https://doi.org/10.3390/rs16183488

Egbert, G. D., & Erofeeva, S. Y. (2002). Efficient inverse modeling of Barotropic Ocean tides. *Journal of Atmospheric and Oceanic Technology*, *19*(2), 183–204. https://doi.org/10.1175/1520-0426(2002)019<0183:eimobo>2.0.co;2

Fer, I., Voet, G., Seim, K. S., Rudels, B., & Latarius, K. (2010). Intense mixing of the Faroe bank channel overflow. *Geophysical Research Letters*, *37*(2). https://doi.org/10.1029/2009gl041924

Firing, E., & Hummon, J. (2010). Shipboard ADCP measurements.

Gula, J., Molemaker, M. J., & McWilliams, J. C. (2016). Topographic generation of submesoscale centrifugal instability and energy dissipation. *Nature Communications*, *7*(1), 12811. https://doi.org/10.1038/ncomms12811

Gula, J., Theetten, S., Cambon, G., & Roullet, G. (2021). Description of the Gigatl simulations. *Zenodo*. https://doi.org/10.5281/zenodo.4948523

Guo, C., Ilicak, M., Fer, I., Darelius, E., & Bentsen, M. (2014). Baroclinic instability of the Faroe Bank Channel overflow. *Journal of Physical Oceanography*, *44*(10), 2698–2717. https://doi.org/10.1175/jpo-d-14-0080.1

Hansen, B., Larsen, K. M., Hátún, H., Olsen, S. M., Gierisch, A. M., Østerhus, S., & Ólafsdóttir, S. R. (2023). The Iceland–Faroe warm-water flow towards the Arctic estimated from satellite altimetry and in situ observations. *Ocean Science*, *19*(4), 1225–1252. https://doi.org/10.5194/os-19-1225-2023

Johns, W. E., Devana, M., Houk, A., & Zou, S. (2021). Moored observations of the Iceland-Scotland overflow plume along the eastern flank of the Reykjanes Ridge. *Journal of Geophysical Research: Oceans*, *126*(8), e2021JC017524. https://doi.org/10.1029/2021jc017524

Kanzow, T., & Zenk, W. (2014). Structure and transport of the Iceland Scotland overflow plume along the Reykjanes Ridge in the Iceland basin. *Deep Sea Research Part I: Oceanographic Research Papers*, *86*, 82–93. https://doi.org/10.1016/j.dsr.2013.11.003

Large, W., & Yeager, S. (2009). The global climatology of an interannually varying air–sea flux data set. *Climate Dynamics*, *33*(2–3), 341–364. https://doi.org/10.1007/s00382-008-0441-3

Larsen, K. M. H., Hansen, B., Hátún, H., Johansen, G. E., Østerhus, S., & Olsen, S. M. (2024). The Coldest and densest overflow branch into the North Atlantic is stable in transport, but warming. *Geophysical Research Letters*, *51*(16), e2024GL110097. https://doi.org/10.1029/2024gl110097

Lozier, M. S., Li, F., Bacon, S., Bahr, F., Bower, A. S., Cunningham, S., et al. (2019). A sea change in our view of overturning in the subpolar North Atlantic. *Science*, *363*(6426), 516–521. https://doi.org/10.1126/science.aau6592

Martínez-Moreno, J., Hogg, A. M., England, M. H., Constantinou, N. C., Kiss, A. E., & Morrison, A. K. (2021). Global changes in oceanic mesoscale currents over the satellite altimetry record. *Nature Climate Change*, *11*(5), 397–403. https://doi.org/10.1038/s41558-021-01006-9

Mashayek, A., Gula, J., Baker, L., Garabato, A. N., Cimoli, L., & Riley, J. (2021). Mountains to climb: On the role of seamounts in upwelling of deep ocean waters. Preprint(Version 1). https://doi.org/10.21203/rs.3.rs-939198/v1

Mason, E., Pascual, A., & McWilliams, J. C. (2014). A new sea surface height–based code for oceanic mesoscale eddy tracking. *Journal of Atmospheric and Oceanic Technology*, *31*(5), 1181–1188. https://doi.org/10.1175/jtech-d-14-00019.1

McPhee, M. G. (1992). Turbulent heat flux in the upper ocean under sea ice. *Journal of Geophysical Research*, *97*(C4), 5365–5379. https://doi.org/10.1029/92jc00239

McPhee, M. G., & Martinson, D. G. (1994). Turbulent mixing under drifting pack ice in the Weddell Sea. *Science*, *263*(5144), 218–221. https://doi.org/10.1126/science.263.5144.218

Meehl, G. A., Goddard, L., Boer, G., Burgman, R., Branstator, G., Cassou, C., et al. (2014). Decadal climate prediction: An update from the trenches. *Bulletin of the American Meteorological Society*, *95*(2), 243–267. https://doi.org/10.1175/bams-d-12-00241.1

Morrow, R., Fu, L.-L., Ardhuin, F., Benkiran, M., Chapron, B., Cosme, E., et al. (2019). Global observations of fine-scale ocean surface topography with the Surface Water and Ocean Topography (SWOT) mission. *Frontiers in Marine Science*, *6*, 232. https://doi.org/10.3389/fmars.2019.00232

Napolitano, D. C., Carton, X., & Gula, J. (2024). Vertical interaction between NBC rings and its implications for South Atlantic water export. *Journal of Geophysical Research: Oceans*, *129*(4), e2023JC020741. https://doi.org/10.1029/2023jc020741

Olsen, S., Hansen, B., Østerhus, S., Quadfasel, D., & Valdimarsson, H. (2016). Biased thermohaline exchanges with the Arctic across the Iceland–Faroe Ridge in ocean climate models. *Ocean Science*, *12*(2), 545–560. https://doi.org/10.5194/os-12-545-2016

Perkins, H., Hopkins, T., Malmberg, S.-A., Poulain, P.-M., & Warn-Varnas, A. (1998). Oceanographic conditions east of Iceland. *Journal of Geophysical Research*, *103*(C10), 21531–21542. https://doi.org/10.1029/98jc00890

Polyakov, I. V., Pnyushkov, A. V., Alkire, M. B., Ashik, I. M., Baumann, T. M., Carmack, E. C., et al. (2017). Greater role for Atlantic inflows on sea-ice loss in the Eurasian basin of the Arctic Ocean. *Science*, *356*(6335), 285–291. https://doi.org/10.1126/science.aai8204

Pörtner, H.-O., Roberts, D. C., Masson-Delmotte, V., Zhai, P., Tignor, M., Poloczanska, E., & Weyer, N. (2019). The ocean and cryosphere in a changing climate. In *IPCC special report on the ocean and cryosphere in a changing climate*. 1155.

Qu, L., Thomas, L., & Gula, J. (2021). Bottom mixing enhanced by tropical storm-generated near-inertial waves entering critical layers in the Straits of Florida. *Geophysical Research Letters*, *48*(15), e2021GL093773. https://doi.org/10.1029/2021gl093773

Ray, R. D. (1999). *A global ocean tide model from TOPEX/POSEIDON altimetry: GOT99.2*. National Aeronautics and Space Administration, Goddard Space Flight Center.

Renault, L., Masson, S., Arsouze, T., Madec, G., & McWilliams, J. C. (2020). Recipes for how to force oceanic model dynamics. *Journal of Advances in Modeling Earth Systems*, *12*(2), e2019MS001715. https://doi.org/10.1029/2019ms001715

Ruan, X., Wenegrat, J. O., & Gula, J. (2021). Slippery bottom boundary layers: The loss of energy from the general circulation by bottom drag. *Geophysical Research Letters*, *48*(19), e2021GL094434. https://doi.org/10.1029/2021gl094434

Saha, S., Moorthi, S., Pan, H.-L., Wu, X., Wang, J., Nadiga, S., et al. (2010). The NCEP climate forecast system reanalysis. *Bulletin of the American Meteorological Society*, *91*(8), 1015–1058. https://doi.org/10.1175/2010bams3001.1

Saunders, P. M. (1996). The flux of dense cold overflow water southeast of Iceland. *Journal of Physical Oceanography*, *26*(1), 85–95. https://doi.org/10.1175/1520-0485(1996)026<0085:tfodco>2.0.co;2

Schubert, R., Vergara, O., & Gula, J. (2023). The open ocean kinetic energy cascade is strongest in late winter and spring. *Communications Earth & Environment*, *4*(1), 450. https://doi.org/10.1038/s43247-023-01111-x

Shchepetkin, A. F., & McWilliams, J. C. (2005). The Regional Oceanic Modeling System (ROMS): A split-explicit, free-surface, topography-following-coordinate oceanic model. *Ocean Modelling*, *9*(4), 347–404. https://doi.org/10.1016/j.ocemod.2004.08.002

Shchepetkin, A. F., & McWilliams, J. C. (2011). Accurate Boussinesq oceanic modeling with a practical, “stiffened” equation of State. *Ocean Modelling*, *38*(1–2), 41–70. https://doi.org/10.1016/j.ocemod.2011.01.010

Shi, J.-R., Santer, B. D., Kwon, Y.-O., & Wijffels, S. E. (2024). The emerging human influence on the seasonal cycle of sea surface temperature. *Nature Climate Change*, *14*(4), 1–9. https://doi.org/10.1038/s41558-024-01958-8

Strehl, A.-M., Våge, K., Smedsrud, L. H., & Barreyre, T. (2024). A 70-year perspective on water-mass transformation in the Greenland Sea: From thermobaric to thermal convection. *Progress in Oceanography*, *227*, 103304. https://doi.org/10.1016/j.pocean.2024.103304

Su, Z., Wang, J., Klein, P., Thompson, A. F., & Menemenlis, D. (2018). Ocean submesoscales as a key component of the global heat budget. *Nature Communications*, *9*(1), 775. https://doi.org/10.1038/s41467-018-02983-w

Tagliabue, A., Lough, A. J., Vic, C., Roussenov, V., Gula, J., Lohan, M. C., et al. (2022). Mechanisms driving the dispersal of hydrothermal iron from the northern Mid Atlantic Ridge. *Geophysical Research Letters*, *49*(22), e2022GL100615. https://doi.org/10.1029/2022gl100615

Tchilibou, M., Carrere, L., Lyard, F., Ubelmann, C., Dibarboure, G., Zaron, E. D., & Arbic, B. K. (2025). Internal tides off the Amazon shelf in the western tropical Atlantic: Analysis of SWOT Cal/Val mission data. *Ocean Science*, *21*(1), 325–342. https://doi.org/10.5194/os-21-325-2025

Thompson, A. F., Lazar, A., Buckingham, C., Garabato, A. C. N., Damerell, G. M., & Heywood, K. J. (2016). Open-ocean submesoscale motions: A full seasonal cycle of mixed layer instabilities from gliders. *Journal of Physical Oceanography*, *46*(4), 1285–1307. https://doi.org/10.1175/jpo-d-15-0170.1

Tsubouchi, T., Våge, K., Hansen, B., Larsen, K. M. H., Østerhus, S., Johnson, C., et al. (2021). Increased ocean heat transport into the Nordic seas and Arctic ocean over the period 1993–2016. *Nature Climate Change*, *11*(1), 21–26. https://doi.org/10.1038/s41558-020-00941-3

Uchida, T., Le Sommer, J., Stern, C., Abernathey, R., Holdgraf, C., Albert, A., et al. (2022). Cloud-based framework for inter-comparing submesoscale permitting realistic ocean models. *Geoscientific Model Development Discussions*, *2022*(14), 1–32. https://doi.org/10.5194/gmd-15-5829-2022

Van Aken, H., & Becker, G. (1996). Hydrography and through-flow in the North-Eastern North Atlantic ocean: The NANSEN project. *Progress in Oceanography*, *38*(4), 297–346. https://doi.org/10.1016/s0079-6611(97)00005-0

Verger-Miralles, E., Mourre, B., Gómez-Navarro, L., Barceló-Llull, B., Casas, B., Cutolo, E., et al. (2024). SWOT enhances small-scale intra-thermocline eddy detection. *Authorea Preprints*. https://doi.org/10.22541/essoar.173315547.75973902/v1

Vic, C., Hascoët, S., Gula, J., Huck, T., & Maes, C. (2022). Oceanic mesoscale cyclones cluster surface Lagrangian material. *Geophysical Research Letters*, *49*(4), e2021GL097488. https://doi.org/10.1029/2021gl097488

Wang, J., Archer, M., Klein, P., & Fu, L.-L. (2025). Global submesoscale ocean dynamics unveiled by Wide-Swath satellite altimetry. https://doi.org/10.21203/rs.3.rs-5177358/v1

Winton, M., Griffies, S. M., Samuels, B. L., Sarmiento, J. L., & Frölicher, T. L. (2013). Connecting changing ocean circulation with changing climate. *Journal of Climate*, *26*(7), 2268–2278. https://doi.org/10.1175/jcli-d-12-00296.1

Wong, A. P., Wijffels, S. E., Riser, S. C., Pouliquen, S., Hosoda, S., Roemmich, D., et al. (2020). Argo data 1999–2019: Two million temperature-salinity profiles and subsurface velocity observations from a global array of profiling floats. *Frontiers in Marine Science*, *7*, 700. https://doi.org/10.3389/fmars.2020.00700

Zhang, X., Liu, L., Fei, J., Li, Z., Wei, Z., Zhang, Z., et al. (2024a). Advances in surface water and ocean topography for fine-scale eddy identification from altimeter sea surface height merging maps. *EGUsphere*, *2024*, 1–19.

Zhang, Z., Miao, M., Qiu, B., Tian, J., Jing, Z., Chen, G., & Zhao, W. (2024b). Submesoscale eddies detected by SWOT and moored observations in the Northwestern Pacific. *Geophysical Research Letters*, *51*(15), e2024GL110000. https://doi.org/10.1029/2024gl110000

Zou, S., Bower, A., Furey, H., Susan Lozier, M., & Xu, X. (2020). Redrawing the Iceland- Scotland overflow water pathways in the North Atlantic. *Nature Communications*, *11*(1), 1890. https://doi.org/10.1038/s41467-020-15513-4

Zou, S., Lozier, S., Zenk, W., Bower, A., & Johns, W. (2017). Observed and modeled pathways of the Iceland Scotland overflow water in the eastern North Atlantic. *Progress in Oceanography*, *159*, 211–222. https://doi.org/10.1016/j.pocean.2017.10.003